Check for updates

Fabrication of water-resistant fluorescent ink using the near-unity photoluminescence quantum yield of CsPbBr₃ doped with NiBr₂†

Dipanwita Roy,[a] Shramana Guha[a] and Somobrata Acharya ⓘ *[a,b]

Doping with transition and alkaline earth metal ions into all-inorganic perovskite nanocrystals (NCs) has attracted attention recently for tuning the photoluminescence quantum yield (PLQY). We report on the hot injection synthesis of nickel ion-doped CsPbBr₃ NCs with near-unity PLQYs. Nickel ions were successfully incorporated into the octahedral environment of CsPbBr₃ NCs, replacing the lead ions. The introduction of nickel ions into CsPbBr₃ NCs substantially eliminates intrinsic defects and halide vacancies for improved structural order and near-unity PLQYs. Benefiting from these unique properties, nickel ion-doped CsPbBr₃ NCs were dispersed in a polymer to prepare an efficient fluorescent ink. The fluorescent ink shows excellent thermal and water stability under harsh environmental conditions. Moreover, the usefulness of the fluorescent ink for security purposes was demonstrated by designing and recognizing a fluorescent QR code. This study reveals that doped CsPbBr₃ NCs can be used to prepare efficient water-resistant fluorescent ink for anti-counterfeiting applications, widening the usefulness of doped all-inorganic perovskite NCs.

1. Introduction

All-inorganic lead halide perovskites (LHPs) CsPbX₃ (X = Br, Cl, I) have attracted enormous research interest recently owing to their excellent physical and optoelectronic properties originating from their direct optical band gap,[1] large optical absorption coefficient,[2,3] long-range diffusion length,[4] high charge carrier mobility,[5] high photoluminescence quantum yield (PLQY),[6] narrow photoluminescence (PL) linewidth,[7] and wide colour gamut.[1–5] These interesting properties bring great potentiality[8–11] towards various optoelectronic applications like photovoltaics,[12,13] light-emitting diodes,[14–16] single-photon sources,[17–19] X-ray scintillators,[20] and lasers.[21] However, the sensitivity of LHPs to oxygen and moisture is an obstacle for realistic applications.[22,23] Structural and surface defects affect their stability in the presence of moisture, light and thermal stress, transforming the pristine nature of the LHPs.[24] To date, several strategies have been adopted to improve the stability of LHP nanocrystals (NCs). These include the use of ammonium

alkyl halides, benzoyl halides and ammonium halides as efficient halide sources,[25–27] fabrication of core–shell structures and encapsulation of NCs using polymers.[28,29] The Pb²⁺ in [PbX₆]⁴⁻ octahedra has a strong effect on the optical and structural properties of LHPs. In the quest for improving optoelectronic properties, doping with metal ions is an effective approach for LHPs. The basic idea is to reduce the numbers of defects and vacancies and to improve the lattice ordering of [PbX₆]⁴⁻ octahedra for enhanced PLQYs.[30–33] Recently, various dopants like transition metals (Mn²⁺, Ni²⁺, Cd²⁺, Co²⁺ *etc.*) and alkaline Earth metals (Ba²⁺, Sr²⁺, Ca²⁺ *etc.*) have been incorporated into CsPbX₃ NCs.[32–37] It is generally observed that doping of perovskite NCs enhances their crystallinity, charge recombination efficiency and PL behaviour with improved PLQYs. Yong *et al.* reported near-unity PLQYs of mixed halide CsPbClₓBr₃₋ₓ NCs (x = 1.5, 2.4, 3) by Ni²⁺ doping.[38] Nickel ions were chosen as the dopant considering their strong preference for octahedral coordination with halide ions. The short-range disorder of the lattice induced intrinsic defects such as halide vacancies, which were substantially eliminated to improve the PLQYs of doped NCs. Zhou *et al.* reported the incorporation of Mn²⁺ into CsPbCl₃ NCs *via* directly inserting [MnCl₆]⁴⁻ octahedra into the perovskite structure during the nucleation and growth processes.[39] The PLQYs of the CsPbCl₃ perovskite reached 40% upon Mn doping. These results demonstrated that the doping strategy potentially enhanced the PL properties of the CsPbX₃ NCs. As a non-activator metal ion, the Ni²⁺

[a]School of Applied and Interdisciplinary Sciences, Indian Association for the Cultivation of Science, Jadavpur, Kolkata 700032, India. E-mail: camsa2@iacs.res.in
[b]Technical Research Centre (TRC), Indian Association for the Cultivation of Science, Kolkata 700032, India
†Electronic supplementary information (ESI) available: FFT, EDX, ICP-AES, TGA, PLQY, and PL spectra of the fluorescent ink. See DOI: https://doi.org/10.1039/d4nr00668b

dopant is attractive due to its electron spin of $S = 1.83$, lack of nuclear spin and weak spin–orbit coupling effect compared to Pb^{2+}.[40,41]

The magnetic dopants can also impart strong magnetization in the host lattice.[40] The smaller ionic radius of Ni^{2+} (69 pm) compared to that of Pb^{2+} (119 pm) contracts the host lattice. Divalent Ni^{2+} ions have a preference for octahedral coordination with halide ions of the perovskite lattice.[41] Ni^{2+} ions with the same iso-valency and coordination mode as Pb^{2+} ions increase the stability of the resulting perovskite lattice structure with improved PL efficiency. Such NCs with high PLQYs and tunable PL wavelengths with narrow full width at half maxima (FWHM) in the visible range are attractive for real-world applications, yet examples are limited. Fluorescent ink is one of the commercial applications used in QR code anti-counterfeiting technologies.[42] To fabricate an ink, highly luminescent perovskite NCs are mixed with the polymer host which acts as an encapsulating agent. Hydrophobicity and thermal stability are the crucial parameters of fluorescent inks prepared with NCs for security purposes.[42–44] In this study, we synthesized Ni^{2+}-doped perovskite $CsPbBr_3$ NCs and compared their optical properties with those of undoped NCs. A near-unity PLQY was achieved by optimizing the Ni^{2+} dopant concentration in the host $CsPbBr_3$ NCs. The crystallinity of the doped NCs was improved compared to that of pristine NCs by increasing the dopant concentration. The high PLQY and enhanced stability of the doped NCs were utilized to prepare fluorescent ink by mixing them with polydimethyl siloxane (PDMS). The high PLQY and narrow FWHM of PL of the doped NCs were retained in the host PDMS. The resulting fluorescent ink showed robust luminescence at elevated temperature. Additionally, the fluorescent ink showed excellent water-resistant properties that are useful for commercial purposes. We demonstrated the stability of the fluorescent ink under harsh environmental conditions and its usefulness for security purposes.

2. Experimental section

2.1. Materials

Cesium carbonate (Cs_2CO_3, 98%, Spectrochem), lead bromide ($PbBr_2$, 98%, Sigma), 1-octadecene (ODE, 90%, Sigma), oleic acid (OA, 90%, Sigma), oleylamine (OLAm, 70%, Sigma), nickel bromide ($NiBr_2$, 98%, Sigma), hexane (Merck), and ethyl acetate (Merck) were used for the synthesis and washing of NCs directly without further purification. All reactions were carried out under a continuous N_2 atmosphere. PDMS (polydimethylsiloxane) was used for ink fabrication.

2.2. Preparation of the cesium oleate (Cs-OA) complex

Cs_2CO_3 (400 mg), oleic acid (1.75 mL), and ODE (15 mL) were taken into a 50 mL round bottom flask and heated to 120 °C under vacuum with vigorous stirring. Then, the temperature of the reaction mixture was raised to 150 °C under an N_2 atmosphere until the solution was clear. This solution was kept under an N_2 atmosphere for high temperature hot-injection synthesis.

2.3. Synthesis of halide perovskite $CsPbBr_3$ NCs

In a 25 mL three-necked round bottom flask, $PbBr_2$ (0.188 mmol) was mixed with OA (500 μL), OLAm (500 μL), and ODE (3 mL) and heated to 120 °C under vacuum for 30 min under continuous stirring conditions. After 30 min of vacuum treatment, the reaction temperature was raised to 160 °C under an N_2 atmosphere. The mixture turned to a clear yellow solution after the dissolution of Pb salts. At 160 °C, 0.6 mL of Cs-OA was injected within the reaction mixture and the reaction was immediately quenched in ice-water. In the case of doped $CsPbBr_3$ NCs, different numbers of moles of $NiBr_2$ salts were added. The as-prepared $CsPbBr_3$ NCs were washed with ethyl acetate at 8500 rpm for 10 min and the solution was then washed with hexane and ethyl acetate and it was dissolved in hexane for further characterization.

2.4. Characterization

A Cary 60 UV-vis spectrophotometer was used for recording UV-vis absorption spectra, photoluminescence (PL) spectra were recorded using a Nanolog spectrofluorometer from HORIBA Jobin Yvon, and temperature-dependent PL spectra were recorded using a FuloroMax-3 spectrometer from HORIBA Jobin Yvon. The PLQY was measured using a calibrated integrated sphere attached to an FL3-2iHR Nanolog spectrofluorometer. X-Ray diffraction (XRD) measurements were performed with a Bruker D8 Advance powder diffractometer using Cu Kα ($\lambda = 1.5418$ Å) as the incident radiation. Transmission electron microscopy (TEM) and high-resolution TEM (HRTEM) images were recorded with a UHR FEG-TEM, JEOL JEM-2100F electron microscope using a 200 kV electron source. A diluted solution of $CsPbBr_3$ and doped NCs were drop-cast onto a carbon-coated copper grid and dried for TEM measurements. To measure the Ni/Pb elemental ratio, an inductively coupled plasma atomic emission spectrometer (ICP-AES, PerkinElmer Optima 2100 DV) was used. The as-synthesized and washed doped and undoped $CsPbBr_3$ NCs were initially digested in concentrated HNO_3. In the next step, they were diluted with Milli-Q water, maintaining a particular concentration for ICP-AES measurements. For time-correlated single photon counting (TCSPC) measurements, the samples were excited at 410 nm using a picosecond diode laser (IBH Nanoled-07) in an IBH Fluorocube apparatus (JY-IBH-5000M). Fluorescence decays were recorded on a Hamamatsu MCP photomultiplier and analysed using DAS6 software. The average life time (τ_{avg}) was calculated from the decay time (τ_n, $n = 1, 2... n$) and normalized pre-exponential factors (A_n, $n = 1, 2,...n$) using the following equation:

$$\tau_{avg} = (\tau_1 \times A_1) + (\tau_2 \times A_2) + ...(\tau_n \times A_n)$$

Thermogravimetric analysis (TGA) was carried out using a Q600, TA Instruments. X-Ray photoelectron spectroscopy (XPS) measurements were carried out using an Omicron electron

spectrometer equipped with an EA125 analyzer and a Mg Kα X-ray source with a photon energy of 1253.6 eV. Nuclear magnetic resonance (NMR) was carried out in d-toluene. ^{133}Cs NMR spectra were recorded using a Bruker 600 MHz spectrometer and the spectra were phase and baseline corrected using MNova software (Mestrelab).

2.5. Fluorescent ink fabrication

Fluorescent ink was prepared by mixing the NCs (5 mg mL^{-1}) with PDMS and painted onto glass or paper. Luminescence was observed under 365 nm UV light. Temperature-dependent PL was measured by placing the film on a hotplate at different temperatures, followed by PL measurements of the film. To measure water stability, a thin film of the ink was immersed in hot water, followed by PL measurements. Contact angle measurement was performed for a thin film of the fluorescent ink using an Ossila contact angle goniometer, L2004A1.

3.   Results and discussion

A general hot-injection synthesis strategy reported by Protesescu *et al.* was followed to synthesize perovskite CsPbBr$_3$ NCs.[4] In a typical synthesis, PbBr$_2$, OA, and OLAm were taken in a round bottom flask heated under vacuum and the Cs-oleate precursor was injected into the reaction mixture at 160 °C. The reaction was quenched in an ice-water bath. The feeding amount of NiBr$_2$ (Ni/Pb molar ratio varies from 0.1 to 0.7) was changed to vary the Ni^{2+} ion concentration for the synthesis of doped CsPbBr$_3$ NCs. TEM images of the as-prepared NCs show a cubic morphology. CsPbBr$_3$ NCs have an average size of 11.7 ± 2 nm (Fig. 1a; inset of Fig. 1a). HRTEM images of the CsPbBr$_3$ NCs reveal an interplanar spacing of 0.21 ± 0.02 nm corresponding to the (011) plane of bulk cubic CsPbBr$_3$ (COD file: 96-153-3064; Fig. 1b). TEM images of the Ni^{2+}-doped CsPbBr$_3$ NCs show a cubic morphology with a size of 7.0 ± 2 nm (Fig. 1c; inset of Fig. 1c). A narrow size distribution was observed for doped NCs in comparison with pristine NCs. This narrow size distribution of the doped NCs compared to the pristine NCs may be attributed to the synergism effect of anions and cations.[45,46] The introduction of Ni^{2+} ions into CsPbBr$_3$ NCs also reduces the interplanar spacing (0.19 ± 0.02 nm) of the (011) plane (Fig. 1d). The fast Fourier transform (FFT) pattern for the doped NCs shows spots corresponding to the (011) and (002) planes similar to those for the undoped CsPbBr$_3$ NCs, suggesting a single-crystalline nature of the NCs (Fig. S1†). Energy dispersive X-ray (EDX) analysis reveals the chemical compositions of the pristine NCs and doped NCs (Fig. S2†). EDX analysis shows the presence of Ni^{2+} in the doped CsPbBr$_3$ NCs and Ni/Pb elemental ratio to be 0.34, which corresponds to the Ni/Pb molar ratio of 0.5 used in the synthesis (Fig. S2†). Quantitative elemental analyses using ICP-AES measurements support the observed atomic ratio of Ni to Pb cations (Table S1†). Furthermore, XPS was employed to investigate the chemical environments of the pristine and doped NCs (Fig. 2). The high-resolution XPS spectrum of pris-
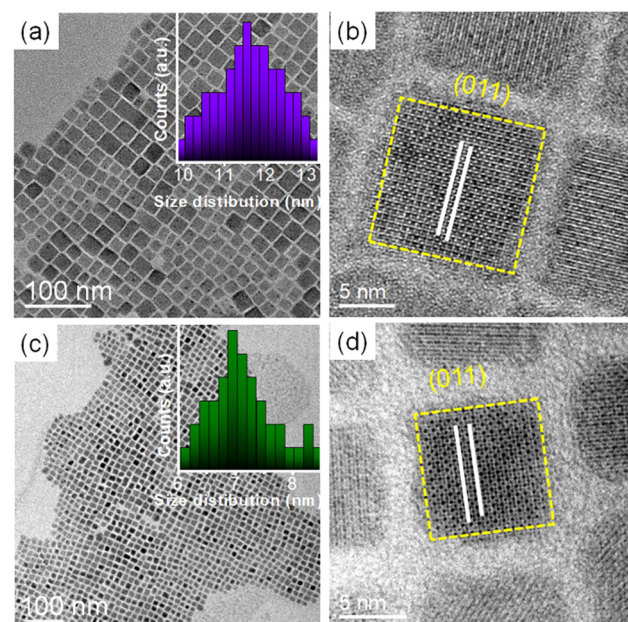

Fig. 1 (a) TEM image of pristine CsPbBr$_3$ NCs with an edge dimension of 11.7 ± 2 nm. The inset shows the corresponding size distribution histogram. (b) High-resolution TEM image of pristine CsPbBr$_3$ NCs of the (011) plane with a lattice spacing of 0.21 ± 0.02 nm. (c) TEM image of Ni^{2+}-doped CsPbBr$_3$ NCs with an edge dimension of 7.02 ± 2 nm. The inset shows the size distribution histogram. (d) High-resolution TEM image of Ni^{2+}-doped CsPbBr$_3$ NCs showing a lattice spacing of 0.19 ± 0.02 nm for the (011) plane.

tine NCs shows Cs 3d doublet peaks at 737.5 eV and 723.5 eV for 3d$_{3/2}$ and 3d$_{5/2}$, respectively (Fig. 2a). The Pb 4f doublet peaks at 142.3 eV and 137.3 eV and Br 3d doublet peaks at 68.36 eV and 67.36 eV have been observed for the pristine NCs (Fig. 2b and c). The XPS spectra of the doped NCs also show peaks corresponding to Cs 3d, Pb 4f and Br 3d orbitals, however, with a shift to higher binding energy, signifying the modified chemical environment of [PbBr$_6$]$^{4-}$ octahedra (Fig. 2a–c).[47,48] A comparison between the pristine and doped NCs suggests an energy shift of ∼0.3 eV for Pb^{2+}, elaborating that Ni^{2+} ions partially displace the Pb^{2+} ionic sites, modifying the chemical environment of [PbBr$_6$]$^{4-}$ octahedra. This is further confirmed by the appearance of two major peaks for the Ni 2p orbital at 869.05 eV and 856.25 eV for 2p$_{1/2}$ and 2p$_{3/2}$, respectively, in the XPS spectrum of the doped NCs (Fig. 2d).[39,43] Increasing the Ni^{2+} content in pristine CsPbBr$_3$ NCs results in a new peak at ∼854.7 eV, which may correlate with the Ni–O bond at the surface due to the Ni^{2+} ligand interactions (Fig. S3†).[40] Considering the fact that ^{133}Cs is sensitive to the local environment, NMR spectroscopy of ^{133}Cs was carried out to probe the local environment of pristine and doped NCs (Fig. S4†). The resonance peak for ^{133}Cs broadens due to the introduction of Ni^{2+} into the perovskite lattice of doped CsPbBr$_3$ NCs, resulting in B-site disorder. TGA shows a mass loss at 176 °C due to the decomposition of organic ligands and a second major loss because of the inorganic core at around 347 °C for the pristine NCs (Fig. S5†).[42] In compari-
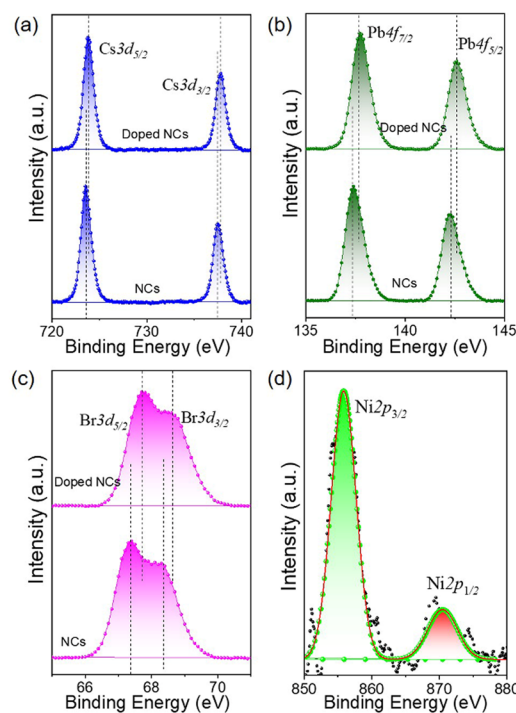
Fig. 2 Survey scans of the oxidation states of elements in the XPS spectra of both pristine and doped CsPbBr$_3$ NCs, which show (a) Cs-3d, (b)Pb-4f, and (c) Br-3d orbitals. The upper and lower panels show the XPS spectra of Ni^{2+}-doped CsPbBr$_3$ and CsPbBr$_3$ NCs, respectively. (d) XPS spectrum of Ni-2p orbitals.

son, the TGA of Ni^{2+}-doped CsPbBr$_3$ NCs shows enhanced thermal stability with a first decomposition temperature at ~347 °C (Fig. S5†).[49]

XRD measurements reveal the formation of a cubic crystal phase for both the pristine and doped NCs (COD file: 96-153-3064) (Fig. 3a). This observation indicates the retention of the host crystallinity after doping with Ni^{2+} in the NCs. However,
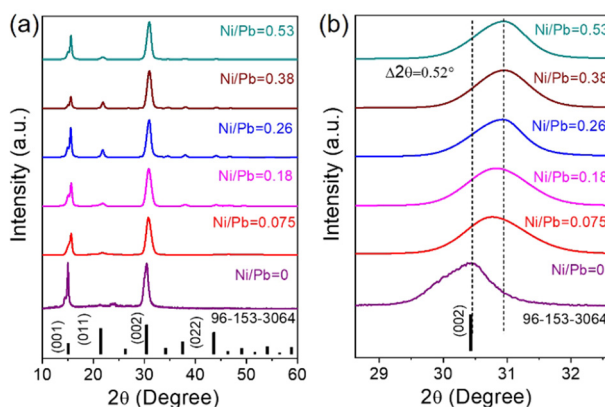
Fig. 3 (a) XRD patterns with changing Ni^{2+} concentration showing the cubic perovskite phase (COD file: 96-153-3064). (b) Enlarged XRD patterns showing a red shift of diffracting peaks with increasing Ni^{2+} concentration. The legends used in the figure represent the elemental ratio of Ni/Pb obtained from ICP-AES.

Ni^{2+} doping brings a change in the characteristic (002) peak of pristine NCs while varying the Ni^{2+} concentration. The diffraction peak at ~30° gradually shifts towards a higher angle upon increasing the Ni^{2+} dopant concentration (Fig. 3b).[50,51] This shift of the (002) peak position towards a higher angle confirms the effective incorporation of Ni^{2+} ions in the pristine CsPbBr$_3$ NCs.[52] Furthermore, we have plotted the lattice parameters *versus* dopant concentration (Ni/Pb ratio obtained from ICP-AES). A linear relationship between the lattice parameters and the composition was obtained (Fig. S6†), which is in good agreement with Vegard's law. The reason for the continuous increase in lattice contraction can be assigned to the decrease in size when the feeding amount of the dopant increases. In the doped CsPbBr$_3$ NCs, the dopant Ni^{2+} ions partially replace the Pb^{2+} ions in the octahedral coordination to form doped perovskite NCs. The smaller size of Ni^{2+} (ionic radius 69 pm) ions in comparison with the Pb^{2+} (ionic radius 119 pm) ions in the octahedral coordination is the key factor, leading to the reduction of the lattice constant upon doping.[52]

To study the dopant effect in the pristine NCs, the optical properties of the NCs were further examined by varying the dopant ion concentration (Fig. 4, Fig. S7, and S8†). The first exciton absorption peak of the pristine CsPbBr$_3$ NCs is located at 513 nm, which is ~13 nm blue shifted when Ni^{2+} is incorporated into the pristine NCs (Fig. 4a). The blue shift of the
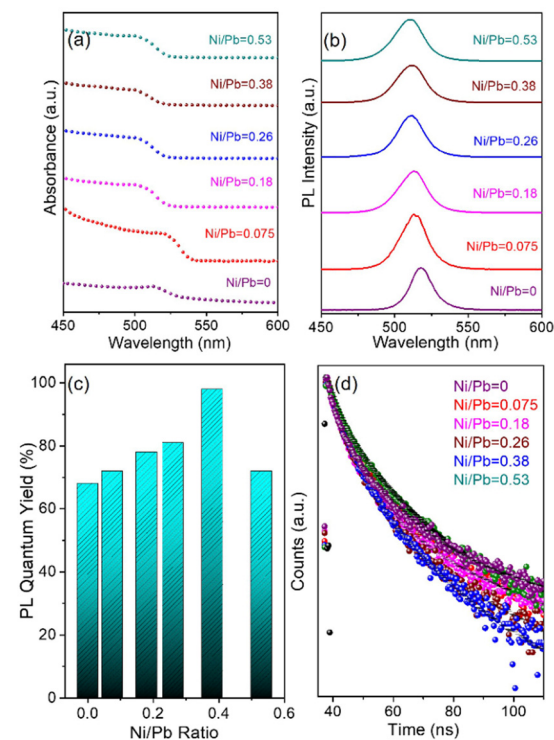
Fig. 4 (a) UV-vis absorption spectra and (b) variation in the PL spectra upon changing the doping concentration of Ni^{2+} ions. (c) PLQYs with increasing dopant concentration. (d) Time decay curves with doping concentration variation. The legends used in the figure represent the elemental ratio of Ni/Pb obtained from ICP-AES.

peak position is attributed to the substitution of larger sized Pb^{2+} ions by smaller sized Ni^{2+} ions in the $[PbX_6]^{4-}$ octahedra.[53–58] Considering the blue shift of the excitonic absorption peak, it can be concluded that the lattice contraction is the key factor for the enhancement of the band gap energy.[56] Additionally, the quantum confinement effect also affects the bandgap energy, which is directly correlated to the smaller size of the doped NCs. The PL peak of the pristine NCs shifts from 516 nm to 511 nm while incorporating the Ni^{2+} ions into the doped NCs. The absence of any dopant related PL peak confirms the minimal effect of doping in the electronic structure of the NCs (Fig. 4b).[55] Importantly, the PL intensity of the doped NCs increases with increasing dopant concentration to a certain extent (Fig. S7†). The NCs exhibit the highest PL intensity for a 0.38 Ni/Pb ratio (obtained from ICP-AES) and the PL intensity decreases further due to an inter-dopant coupling-induced self-quenching effect upon the introduction of excess Ni dopants.[50–53] Notably, Ni^{2+} doping resulted in an increased PL intensity. We found that the PLQY was increased from 68% for the pristine NCs to 98% for the Ni^{2+}-doped NCs with a 0.38 Ni/Pb ratio (Fig. 4c, and Table S2†). Further increase of the Ni^{2+} concentration resulted in a decrease of the PLQY to 72%. The enhancement of the PLQY reveals the reduced non-radiative recombination following the PL decay path.[20] A low dopant concentration can minimize any adverse effects on the structure and enhance the luminescence properties by eliminating structural defects of the doped NCs (Table S3†). However, the use of a high dopant concentration may form an alloyed composition with the host NCs, forming additional mid-gap states.[59] Compared to the pristine NCs, Ni^{2+} doping heals the defect states, leading to PL enhancement. The excess Ni^{2+} leads to self-quenching in the octahedral coordination of NCs. To investigate the photophysical properties of doped NCs, we have carried out TCSPC measurements of the pristine and doped NCs (Fig. 4d, and Table S4†). The average PL lifetime of the NCs initially decreases with increasing dopant concentration and reaches a maximum value for the highest dopant concentration. The initial reduction of the average PL lifetime is attributed to the reduced defect states upon doping, which eliminates the non-radiative pathways for faster decay. However, an excess amount of dopant creates defect states in the crystal structure and increases the halide vacancies.[56] Due to the formation of new vacancy states by halide ions, the PLQY decreases with increasing concentration of Ni^{2+} ions.[22] We have calculated the radiative decay rates, which confirm that the radiative decay rate increases with Ni^{2+} doping and decreases after reaching a maximum value (Table S5†). Also, the decrease in non-radiative decay rate clearly supports the suppression of the non-radiative channel upon doping. Hence, the maximum solubility for Ni^{2+} concentration with ~5.6% (Ni/Pb = 0.38 from ICP-AES) was achieved upon introducing the Ni dopants into $CsPbBr_3$ NCs.

The high PLQY of NCs upon doping offers an attractive opportunity for anti-counterfeiting and security applications. To promote these applications, the as-synthesized doped NCs were mixed with PDMS to prepare an effective fluorescent ink.[57,58] We used doped NCs with the highest PLQY (Ni/Pb = 0.38) in PDMS to prepare the fluorescent ink. Since PDMS is a highly transparent material, it doesn't affect the optical properties of NCs radically. The PL maximum remains almost the same upon incorporation of the NCs into a polymer (Fig. 5a). Both the undoped NCs and doped NCs incorporated into PDMS show an intense green luminescence (inset of Fig. 5a). Since the perovskite NCs are highly sensitive to environmental changes, we examined the stability of the ink at different temperatures. Notably, the PL of the pristine $CsPbBr_3$ NCs quenches completely at 80 °C (Fig. S9a†). The PL of the Ni^{2+}-doped NCs also quenches upon increasing the temperature; however, they still retain 11% of their original intensity at 80 °C (Fig. S9b†). In comparison with the pristine NCs, for doped NCs, the fluorescent ink shows much improved PL stability upon increasing the temperature. The PL retains 60% of its original intensity at 80 °C and the PL of the ink can be detected at an elevated temperature of up to 160 °C (Fig. 5b). The stability under higher thermal conditions is the major advantage of the fluorescent ink of these perovskite NCs. Furthermore, we prepared a thin film of the fluorescent ink on a glass substrate by the doctor blading method. The thin film was placed on a hot plate and several heating–cooling cycles were conducted between 150 °C and 30 °C. It was observed that the ink retained its PL intensity for several heating–cooling cycles (Fig. 5c). This kind of PL sustainability is ideal for anti-counterfeiting applications. Fig. S10† shows photographs of a thin film of ink on a glass slide in daylight and under UV light after conducting the heating–cooling cycles. The thin film shows an intense green colour upon UV exposure. Furthermore, the effect of moisture in the fluorescent ink film was tested by measuring the contact angle. A water droplet placed on the
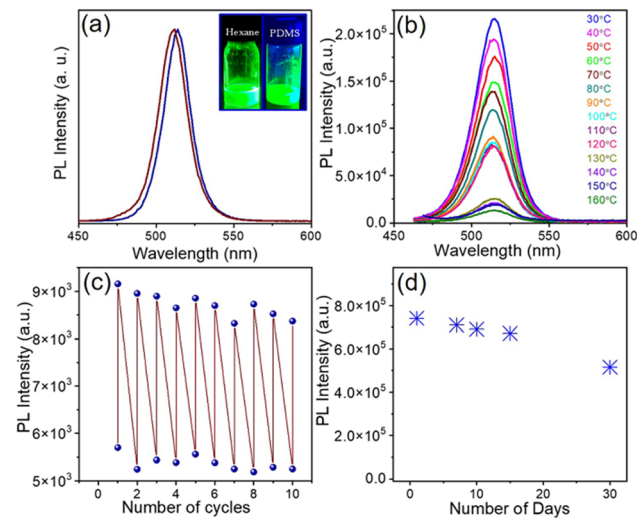

Fig. 5 (a) PL spectra of Ni^{2+}-doped $CsPbBr_3$ NCs in hexane (maroon) and PDMS (royal blue). (b) PL spectra of a thin film of the ink at different temperatures showing thermal stability. (c) Heating–cooling cycles at 150 °C and 30 °C showing the reversible fluorescence cycles of the ink. (d) PL intensity in water for days showing the water resistivity properties of the ink.
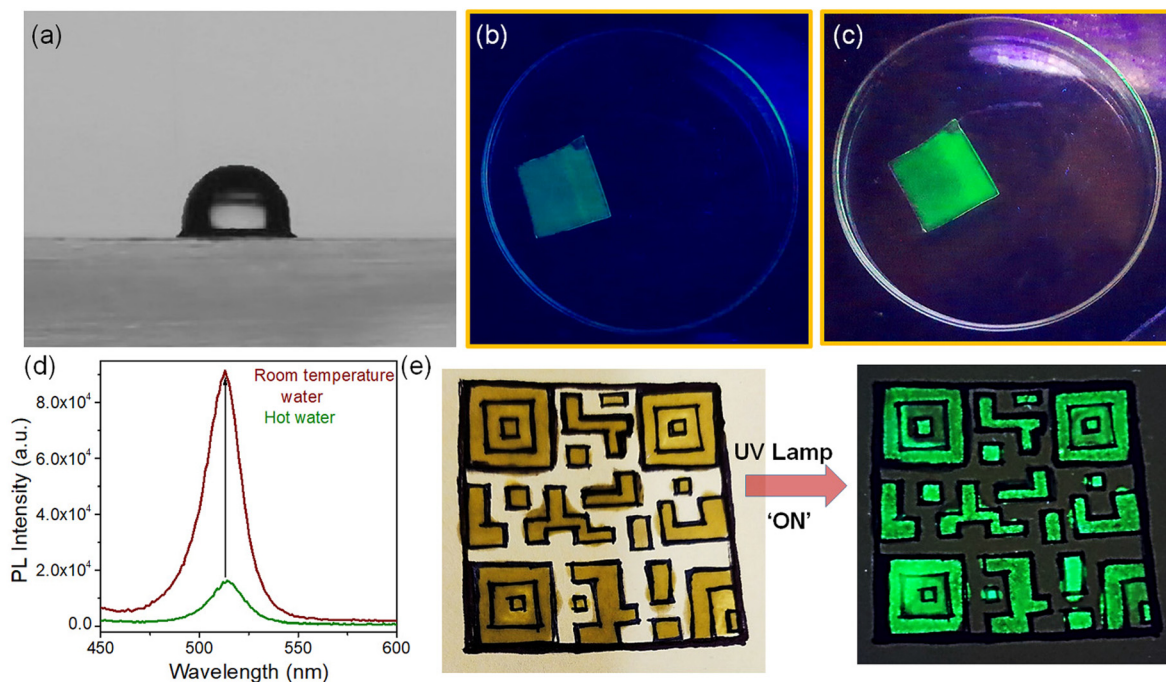
Fig. 6 (a) Study of the contact angle of a water droplet on a thin film of the fluorescent ink. Luminescence images of the film under exposure to a UV lamp at 365 nm (b) in hot water and (c) at room temperature. (d) Enhancement of PL intensity after exposing the film in hot water to room temperature water. (e) Anti-counterfeiting effect for a QR code which clearly shows the proper visibility under illumination with a UV lamp.

thin film of ink shows a contact angle of 91.53°, revealing the hydrophobic nature of the ink (Fig. 6a). The hydrophobic nature of the thin film of the ink inspired us to examine the stability in water. To test the stability in water, the thin film of ink was immersed in water in a Petri dish for several days. The luminescence of the resulting thin film was tested by taking photographs under UV illumination (Fig. S11†) and by measuring PL spectra over an increasing number of days (Fig. 5d; and Fig. S11†). The thin film of the ink retained its PL intensity after 30 days in water. Furthermore, we placed the thin film of the ink in hot water (Fig. 6b). The ink film showed a feeble green colour with the naked eye upon UV exposure. Correspondingly, a weak PL was detectable (Fig. 6d). Interestingly, the same film, when placed in room temperature water, showed an intense green colour upon UV exposure (Fig. 6c). The PL intensity increased by 5-fold when the thin film of the ink was transferred from the hot water to room temperature water (Fig. 6d). Importantly, the moisture stability of the thin film of the ink shown here can be applied for effective anti-counterfeiting applications. We created an arbitrary QR code and filled the characters with the ink (Fig. 6e). The bright green luminescence is visible under the UV illumination of the QR code (Fig. 6e). This observation suggests that the ink can be used to design a fluorescent QR code and QR code recognizer. These observations further demonstrate that the Ni^{2+}-doped NCs with narrow FWHM and improved PL properties are stable under harsh environmental conditions, expanding their potential applications in water resistant fluorescent ink for security purposes.

4. Conclusion

In conclusion, we have reported on the doping of $CsPbBr_3$ NCs with Ni^{2+} ions to obtain single colour green luminescence with near-unity PLQYs. Transition metal Ni^{2+} replaces the Pb^{2+} from the host lattice of perovskite $CsPbBr_3$ NCs. Incorporation of Ni^{2+} in the host NCs retained the crystal structure and stability of the NCs. The high PLQYs along with robust stability of the doped NCs were utilized to prepare a fluorescent ink by mixing them with PDMS. The resulting fluorescent ink shows a hydrophobic nature and high moisture stability. Furthermore, the ink retains its PL intensity for several heating–cooling cycles at elevated temperatures. The robust water resistance properties of the ink were utilized to design a fluorescent QR code and QR code recognizer. This result highlights the importance of doped perovskite NCs towards the fabrication of highly sustainable luminescent ink.

Conflicts of interest

There are no conflicts to declare.

Acknowledgements

References

1 Q. A. Akkerman, V. D'Innocenzo, S. Accornero, A. Scarpellini, A. Petrozza, M. Prato and L. Manna, *J. Am. Chem. Soc.*, 2015, **137**, 10276–10281.

2 G. Nedelcu, L. Protesescu, S. Yakunin, M. I. Bodnarchuk, M. J. Grotevent and M. V. Kovalenko, *Nano Lett.*, 2015, **15**, 5635–5640.

3 A. Swarnkar, R. Chulliyil, V. K. Ravi, M. Irfanullah, A. Chowdhury and A. Nag, *Angew. Chem.*, 2015, **127**, 15644–15648.

4 L. Protesescu, S. Yakunin, M. I. Bodnarchuk, F. Krieg, R. Caputo, C. H. Hendon, R. X. Yang, A. Walsh and M. V. Kovalenko, *Nano Lett.*, 2015, **15**, 3692–3696.

5 Z. Li, L. Kong, S. Huang and L. Li, *Angew. Chem.*, 2017, **129**, 8246–8250.

6 F. Liu, Y. Zhang, C. Ding, S. Kobayashi, T. Izuishi, N. Nakazawa, T. Toyoda, T. Ohta, S. Hayase, T. Minemoto, K. Yoshino, S. Dai and Q. Shen, *ACS Nano*, 2017, **11**, 10373–10383.

7 J. Pan, Y. Shangf, J. Yin, M. De Bastiani, W. Peng, I. Dursun, L. Sinatra, A. M. El-Zohry, M. N. Hedhili, A.-H. Emwas, O. F. Mohammed, Z. Ning and O. M. Bakr, *J. Am. Chem. Soc.*, 2018, **140**, 562–565.

8 J.-H. Im, I. H. Jang, N. Pellet, M. Grätzel and N. G. Park, *Nat. Nanotechnol.*, 2014, **9**, 927–932.

9 F. X. Xie, D. Zhang, H. Su, X. Ren, K. S. Wong, M. Grätzel and W. C. H. Choy, *ACS Nano*, 2015, **9**, 639–946.

10 F. Fu, L. Kranz, S. Yoon, J. Löckinger, T. Jäger, J. Perrenoud, T. Feurer, C. Gretener, S. Buecheler and A. N. Tiwari, *Phys. Status Solidi A*, 2015, **212**, 2708–2717.

11 D. Liu, L. Wu, C. Li, S. Ren, J. Zhang, W. Li and L. Feng, *ACS Appl. Mater. Interfaces*, 2015, **7**, 16330–16337.

12 S. Cho, J. Kim, S. M. Jeong, M. J. Ko, J. S. Lee and Y. Kim, *Chem. Mater.*, 2020, **32**, 8808–8818.

13 Y. Xu, P. Niu, L. Zhang, Z. Wen, S. Cheng, M. Lyu and J. Zhu, *Nanoscale*, 2023, **15**, 9691.

14 J. Song, J. Li, X. Li, L. Xu, Y. Dong and H. Zeng, *Adv. Mater.*, 2015, **27**, 7162–7167.

15 X. Li, Y. Wu, S. Zhang, B. Cai, Y. Gu, J. Song and H. Zeng, *Adv. Funct. Mater.*, 2016, **26**, 2435–2445.

16 J. Pan, L. N. Quan, Y. Zhao, W. Peng, B. Murali, S. P. Sarmah, M. Yuan, L. Sinatra, N. M. Alyami, J. Liu, E. Yassitepe, Z. Yang, O. Voznyy, R. Comin, M. N. Hedhili, O. F. Mohammed, Z. H. Lu, D. H. Kim, E. H. Sargent and O. M. Bakr, *Adv. Mater.*, 2016, **28**, 8718–8725.

17 Y.-S. Park, S. Guo, N. S. Makarov and V. I. Klimov, *ACS Nano*, 2015, **9**, 10386–10393.

18 F. Hu, H. Zhang, C. Sun, C. Yin, B. Lv, C. Zhang, W. W. Yu, X. Wang, Y. Zhang and M. Xiao, *ACS Nano*, 2015, **9**, 12410–12416.

19 G. Rainò, G. Nedelcu, L. Protesescu, M. I. Bodnarchuk, M. V. Kovalenko, R. F. Mahrt and T. Stoferle, *ACS Nano*, 2016, **10**, 2485–2490.

20 Q. Chen, J. Wu, X. Ou, B. Huang, J. Almutlaq, A. A. Zhumekenov, X. Guan, S. Han, L. Liang, Z. Yi, J. Li, X. Xie, Y. Wang, Y. Li, D. Fan, D. B. L. Teh, A. H. All, O. F. Mohammed, O. M. Bakr, T. Wu, M. Bettinelli, H. Yang, W. Huang and X. Liu, *Nature*, 2018, **561**, 88–93.

21 Y. Wang, X. Li, J. Song, L. Xiao, H. Zeng and H. Sun, *Adv. Mater.*, 2015, **27**, 7101–7108.

22 A. Dualeh, N. Tétreault, T. Moehl, P. Gao, M. K. Nazeeruddin and M. Grätzel, *Adv. Funct. Mater.*, 2014, **24**, 3250–3258.

23 J. Su, D. P. Chen and C. T. J. Lin, *Cryst. Growth*, 2015, **422**, 75–79.

24 S. Paul and S. Acharya, *ACS Energy Lett.*, 2022, **7**, 2136–2155.

25 M. Imran, V. Caligiuri, M. Wang, L. Goldoni, M. Prato, R. Krahne, L. De Trizio and L. Manna, *J. Am. Chem. Soc.*, 2018, **140**, 2656–2664.

26 E. Yassitepe, Z. Yang, O. Voznyy, Y. Kim, G. Walters, J. A. Castanẽda, P. Kanjanaboos, M. Yuan, X. Gong, F. Fan, J. Pan, S. Hoogland, R. Comin, O. M. Bakr, L. A. Padilha, A. F. Nogueira and E. H. Sargent, *Adv. Funct. Mater.*, 2016, **26**, 8757–8763.

27 J. Pradhan, P. Moitro, U. B. Das, P. Mondal, G. S. Kumar, U. K. Ghorai, S. Acharya and S. Bhattacharya, *Chem. Mater.*, 2020, **32**, 7159–7171.

28 Q. Zhong, M. Cao, H. Hu, D. Yang, M. Chen, P. Li, L. Wu and Q. Zhang, *ACS Nano*, 2018, **12**, 8579–8587.

29 S. Q. Lou, T. T. Xuan, C. Y. Yu, M. M. Cao, C. Xia, J. Wang and H. L. Li, *J. Mater. Chem. C*, 2017, **5**, 7431–7435.

30 S. Zou, Y. Liu, J. Li, C. Li, R. Feng, F. Jiang, Y. Li, J. Song, H. Zeng, M. Hong and X. Chen, *J. Am. Chem. Soc.*, 2017, **139**, 11443–11450.

31 A. Swarnakar, W. J. Mir and A. Nag, *ACS Energy Lett.*, 2018, **3**, 286–289.

32 E. Akman, T. Ozturk, W. Xiang, F. Sadegh, D. Prochowicz, M. M. Tavakoli, P. Yadav, M. Yilmaz and S. Akin, *Energy Environ. Sci.*, 2023, **16**, 372–403.

33 A. P. Litvin, I. V. Margaryan, W. Yin, X. Zhang, W. Zheng and A. L. Rogach, *Adv. Opt. Mater.*, 2024, **12**, 2301001.

34 S. D. Adhikari, R. K. Behera, S. Bera and N. Pradhan, *J. Phys. Chem. Lett.*, 2019, **10**, 1530–1536.

35 J. K. Chen, J. P. Ma, S. Q. Guo, Y. M. Chen, Q. Zhao, B. B. Zhang, Z. Y. Li, Y. Zhou, J. S. Hou, Y. Kuroiwa, C. Moriyoshi, O. M. Bakr, J. Y. Zhang and H. T. Sun, *Chem. Mater.*, 2019, **31**, 3974–3983.

36 W. Z. Xu, L. Y. Zheng, X. T. Zhang, Y. Cao, T. Y. Meng, D. Z. Wu, L. Liu, W. P. Hu and X. Gong, *Adv. Energy Mater.*, 2018, **8**, 1703178.

37 H. Shao, X. Bai, H. Cui, G. Pan, P. Jing, S. Qu, J. Zhu, Y. Zhai, B. Dong and H. Song, *Nanoscale*, 2018, **10**, 1023–1029.

38 Z.-J. Yong, S.-Q. Guo, J.-P. Ma, J.-Y. Zhang, Z.-Y. Li, Y.-M. Chen, B.-B. Zhang, Y. Zhou, J. Shu, J.-L. Gu, L.-R. Zheng, O. M. Bakr and H.-T. Sun, *J. Am. Chem. Soc.*, 2018, **140**, 9942–9951.

39 S. Zhou, Y. Zhu, J. Zhong, F. Tian, H. Huang, J. Chen and D. Chen, *Nanoscale*, 2019, **11**, 12465–12470.

40 A. Shapiro, M. W. Heindl, F. Horani, M. H. Dahan, J. Tang, Y. Amouyal and E. Lifshitz, *J. Phys. Chem. C*, 2019, **123**, 24979–24987.

41 H. Kim, S. R. Bae, T. H. Lee, H. Lee, H. Kang, S. Park, H. W. Jang and S. Y. Kim, *Adv. Funct. Mater.*, 2021, **31**, 2102770.

42 J. Shi, Y. Tian, W. Gao, M. Xu, Y. Wu and W. Ge, *ACS Appl. Electron. Mater.*, 2021, **3**, 1413–1421.

43 L. Xu, J. Chen, J. Song, J. Li, J. Xue, Y. Dong, B. Cai, Q. Shan, B. Han and H. Zeng, *ACS Appl. Mater. Interfaces*, 2017, **9**, 26556–26564.

44 G. Jiang, C. Guhrenz, A. Kirch, L. Sonntag, C. Bauer, X. Fan, J. Wang, S. Reineke, N. Gaponik and A. Eychmüller, *ACS Nano*, 2019, **13**, 10386–10396.

45 G. Pan, X. Bai, W. Xu, X. Chen, Y. Zhai, J. Zhu, H. Shao, N. Ding, L. Xu and B. Dong, *ACS Appl. Mater. Interfaces*, 2020, **12**, 14195–14202.

46 J. Zhu, X. Yang, Y. Zhu, Y. Wang, J. Cai, J. Shen, L. Sun and C. Li, *J. Phys. Chem. Lett.*, 2017, **8**, 4167–4171.

47 M. Liu, G. Zhong, Y. Yin, J. Miao, K. Li, C. Wang, X. Xu, C. Shen and H. Meng, *Adv. Sci.*, 2017, **4**, 1700335.

48 T. Cai, J. Wang, W. Li, K. Hills-Kimball, H. Yang, Y. Nagaoka, Y. Yuan, R. Zia and O. Chen, *Adv. Sci.*, 2020, **7**(18), 2001317.

49 M. Kulbak, S. Gupta, N. Kedem, I. Levine, T. Bendikov, G. Hodes and D. Cahen, *J. Phys. Chem. Lett.*, 2016, **7**, 167–172.

50 M. Pazoki, T. J. Jacobsson, A. Hagfeldt, G. Boschloo and T. Edvinsson, *Phys. Rev. B*, 2016, **93**, 144105.

51 J. Cao, S. X. Tao, P. A. Bobbert, C.-P. Wong and N. Zhao, *Adv. Mater.*, 2018, **30**, 1707350.

52 N. Mondal, A. De and A. Samanta, *ACS Energy Lett.*, 2019, **4**, 32–39.

53 R. Begum, M. R. Parida, A. L. Abdelhady, B. Murali, N. M. Alyami, G. H. Ahmed, M. N. Hedhili, O. M. Bakr and O. F. Mohammed, *J. Am. Chem. Soc.*, 2017, **139**, 731–737.

54 V. der Stam, W. Geuchies, J. J. Altantzis, T. Van Den Bos, K. H. Meeldijk, J. D. Van Aert, S. Bals, S. Vanmaekelbergh and C. de Mello Donega, *J. Am. Chem. Soc.*, 2017, **139**, 4087–4097.

55 T. Cai, H. Yang, K. Hills-Kimball, J.-P. Song, H. Zhu, E. Hofman, W. Zheng, B. M. Rubenstein and O. Chen, *J. Phys. Chem. Lett.*, 2018, **9**, 7079–7084.

56 D. Roy, P. K. Sarkar, A. Dalui, U. K. Ghorai, D. K. Gupta and S. Acharya, *J. Mater. Chem. C*, 2021, **9**, 8066–8075.

57 Y. Hu, X. Zhang, C. Yang, J. Liab and L. Wang, *RSC Adv.*, 2019, **9**, 33017–33022.

58 W. Ge, J. Shi, Y. Tian, M. Xu, Y. Wu and Y. Li, *J. Alloys Compd.*, 2021, **865**, 158768.

59 A. H. Khan, A. Dalui, S. Mukherjee, C. U. Segre, D. D. Sarma and S. Acharya, *Angew. Chem., Int. Ed.*, 2015, **54**, 2643–2648.